Beyond the limits: Pushing the boundaries of polyimide triboelectric nanogenerator performance at elevated temperatures

Wu, Peng; Shirvanimoghaddam, Kamyar; Leon, Ronald T.; Ravi Anusuyadevi, Prasaanth; Taheri, Peyman; Gonugunta, Prasad; Ellis, Amanda V.; Naebe, Minoo

DOI
10.1016/j.cej.2025.161809

Publication date
2025

Document Version
Final published version

Published in
Chemical Engineering Journal

Citation (APA)
Wu, P., Shirvanimoghaddam, K., Leon, R. T., Ravi Anusuyadevi, P., Taheri, P., Gonugunta, P., Ellis, A. V., & Naebe, M. (2025). Beyond the limits: Pushing the boundaries of polyimide triboelectric nanogenerator performance at elevated temperatures. *Chemical Engineering Journal*, *512*, Article 161809. https://doi.org/10.1016/j.cej.2025.161809

Chemical Engineering Journal 512 (2025) 161809

Contents lists available at ScienceDirect

Chemical Engineering Journal

journal homepage: www.elsevier.com/locate/cej

Beyond the limits: Pushing the boundaries of polyimide triboelectric nanogenerator performance at elevated temperatures

Peng Wu [a], Kamyar Shirvanimoghaddam [b,*], Ronald T. Leon [c], Ir. Prasaanth Ravi Anusuyadevi [d], Peyman Taheri [d], Prasad Gonugunta [d], Amanda V. Ellis [c], Minoo Naebe [a,*]

[a] Institute for Frontier Materials, Deakin University, Waurn Ponds, Victoria 3216, Australia
[b] School of Fashion and Textiles, RMIT University, Brunswick, Victoria 3056, Australia
[c] School of Chemical and Biomedical Engineering, The University of Melbourne, Parkville, Victoria 3010, Australia
[d] Department of Materials Science and Engineering, Delft University of Technology, Delft 2628 CD, the Netherlands

ARTICLE INFO

Keywords:
Energy harvesting
Triboelectric nanogenerator
Polyimide nanofibers
Smart textiles
High temperature environment

ABSTRACT

This research presents a novel investigation into the intricate relationship between temperature and the performance of polymeric triboelectric nanogenerators experimentally and theoretically. A comprehensive investigation has been conducted to delve into the underlying mechanisms governing the temperature dependence of a triboelectric nanogenerator. The study centers on a meticulously fabricated triboelectric nanogenerator using a polyimide (PI) nanofiber membrane and encompasses a broad temperature spectrum, analyzing behavior at both room temperature and elevated temperatures. The developed PI nanofiber membrane functions as a versatile platform for converting mechanical energy into electrical with potential to harvest energy even from ultra-low frequency movements like the human pulse or the act of scratching. Additionally, the material boasts a sophisticated triboelectric response strategy. This means it exhibits its peak performance within a specific temperature range, optimizing energy conversion efficiency under these conditions. Open circuit voltage (VOC) reaches 11.76 V at 160 °C, an 84.4 % improvement compared to room temperature. A Kelvin probe force microscopy (KPFM) and fast Fourier transform (FFT) analyses have been performed for the first time to decouple the energy conversion mechanism, confirming its primary dependence on triboelectricity. A comprehensive theoretical study explores the working mechanisms of contact electrification (CE) and the triboelectric effect (TE) during temperature elevation in these nanogenerators (TENGs). This work highlights the potential of PI nanofibers as high-performance, flexible nanogenerators, particularly for applications requiring operation in smart, high-temperature environments. The emphasis on decoupling the mechanism through novel techniques and a theoretical framework on the temperature dependence strengthens the originality and contribution of the study.

1. Introduction

The energy crisis has long been a significant global concern. Renewable energies, defined as energy derived from sources like solar, wind, and hydropower, stand out as the ideal and environmentally friendly solutions. Currently, advanced infrastructures harness these renewable energies, contributing to 28.6 % of global energy consumption [1]. Despite this progress, a substantial amount of energy in our environment remains untapped, such as that from moving vehicles [2], acoustic wave [3] and walking step [4], Consequently, there is a meaningful challenge for researchers and engineers to develop technologies that harvest these dissipated renewable energies. The evolution of small, smart, and portable electronic devices has revealed limitations in conventional batteries, including their finite lifespan, storage capacity, and the need for regular recharging [5]. This has spurred a demand for revolutionary power solutions in these fields.

Piezoelectric nanogenerators (PENGs) and triboelectric nanogenerators (TENGs) have garnered substantial interest in recent years due to their potential applications in emerging fields such as the Internet of Things (IoT) [6], smart devices, and wearable electronics [7–9]. Wang et al [10,11] first reported these technologies in 2006.

PENGs convert vibrational energy into electric energy based on the piezoelectric properties of materials. Common materials used in PENGs include ZnO [10,12], lead zirconate titanate (PZT) [13], $BaTiO_3$ [14]

---

* Corresponding authors.
E-mail addresses: Kamyar.shirvani.moghaddam@rmit.edu.au (K. Shirvanimoghaddam), minoo.naebe@deakin.edu.au (M. Naebe).

https://doi.org/10.1016/j.cej.2025.161809
Received 12 January 2025; Received in revised form 17 March 2025; Accepted 19 March 2025

and polyvinylidene fluoride(PVDF) [15,16]. While inorganic piezoelectric materials exhibit promising performance [17–19], their brittleness, fragility, and toxicity limit applications in wearable electronics, foldable monitoring, and biomedical sensors. In contrast, PVDF and its co-polymers, representative polymer-based piezoelectric materials, have found applications in these areas [20].

TENGs, on the other hand, relies on the triboelectricity of materials. Triboelectricity is commonly described as electrification effect induced by contact of two different materials. It is a common occurrence in our daily live, for example, during dry seasons, individuals frequently experience electric shocks when they contact with others. The physical principle for this phenomenon is called CE. Generally, triboelectricity is caused by changes in the electron states at the interface of materials [21–23]. Due to variations in the binding energies of outer electrons for different atoms and molecules, electrons undergo transfer when different materials come into contact, leading to changes in the electrical environment and thereby triggering electric signals. This type of electrical signal also represents a form of energy, which can be collected using designed circuits to serve as power sources for microelectronics [24–28], known as energy harvesting applications. Additionally, its capability to generate specific signals based on different external environments can be utilized to create sensors [29–33]. Given its dual functionality in power generation and signal excitation, it holds significant potential for applications in the IoT [34].

Electrospinning is a versatile technique used to produce nanofibers from polymer solutions or melts by applying a high-voltage electric field, enabling the creation of materials with high surface area and diverse applications in filtration, tissue engineering, and energy [7,35–41]. Recent studies indicate that polymer nanofiber membranes, fabricated using electrospinning technology, exhibit superior mechanical–electrical energy conversion ability compared to their bulk counterparts prepared by conventional methods [42,43]. Nanogenerators consisting of polymer materials such as PVDF [7,38,39,44], P(VDF-TrFE) [15,37], PVA [45], and even amorphous polymer polyacrylonitrile (PAN) [46] nanofibers have demonstrated extraordinary voltage output. The enhanced piezoelectricity of PVDF is attributed to the increased beta crystal phase content after the electrospinning process. However, the mechanism by which the electrospinning process enhances the energy conversion performance of poor piezoelectric materials, such as PAN and PI, requires further explanation. Moreover, developing flexible nanogenerators with high operating temperature capabilities would unlock novel applications in aerospace, power production, and firefighter outfits [47,48]. Existing polymer-based piezoelectric materials fail at high temperatures (e.g., 300 ℃) because of their low Curie temperature [49]. Although efforts have been made to increase the high-temperature resistance of piezoelectric polymers, including crosslinking the polymer chain [50], increasing polymer crystallinity [51], and incorporating inorganic fillers [52], progress has not been ideal [53].

PI are high-performance polymers known for their excellent thermal stability, chemical resistance, and mechanical properties [54]. PI is the polymer containing imide groups. The aromatic PI family is one of the most commercially successful materials widely used in electronics, aerospace and military field due to their excellent thermal stability, chemical resistance, and mechanical properties [55]. PI is also used in the field of TENG due to its good surface electronegativity [56–58]. Currently, the assessment of a material's triboelectric response capability involves the use of triboelectric charge density (TECD). This is a method introduced by the Wang's team [59] in 2019, which shows practical and instructive significance. They used mercury as a general reference to conduct TECD performance tests on over 50 different materials, ranking them based on their performance. From Table 1, it can be observed that polymers generally exhibit higher TECD values. Among them, Viton fluoroelastomer rubber has the highest average TECD of $-148.20\ \mu\text{Cm}^{-2}$ among the tested materials, making it the strongest TECD. Common materials such as PTFE, PDMS, and PI also achieved TECD values of $-113.06\ \mu\text{Cm}^{-2}$, $-102.05\ \mu\text{Cm}^{-2}$, and $-92.88\ \mu\text{Cm}^{-2}$, respectively. Adding the material's max service temperature and mechanical performance to this evaluation table allows for a more comprehensive assessment of the materials. Based on this table, we can

Table 1
The triboelectric charge density (TECD) [59], maximum service temperature and tensile strength of majority of triboelectric materials.

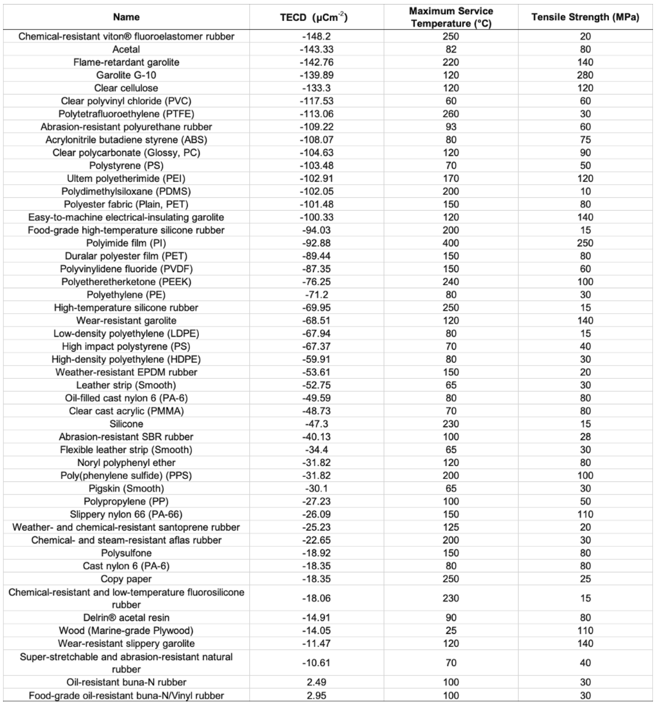

Name	TECD (μCm^{-2})	Maximum Service Temperature (°C)	Tensile Strength (MPa)
Chemical-resistant viton® fluoroelastomer rubber	-148.2	250	20
Acetal	-143.33	82	80
Flame-retardant garolite	-142.76	220	140
Garolite G-10	-139.89	120	280
Clear cellulose	-133.3	120	120
Clear polyvinyl chloride (PVC)	-117.53	60	60
Polytetrafluoroethylene (PTFE)	-113.06	260	30
Abrasion-resistant polyurethane rubber	-109.22	93	60
Acrylonitrile butadiene styrene (ABS)	-108.07	80	75
Clear polycarbonate (Glossy, PC)	-104.63	120	90
Polystyrene (PS)	-103.48	70	50
Ultem polyetherimide (PEI)	-102.91	170	120
Polydimethylsiloxane (PDMS)	-102.05	200	10
Polyester fabric (Plain, PET)	-101.48	150	80
Easy-to-machine electrical-insulating garolite	-100.33	120	140
Food-grade high-temperature silicone rubber	-94.03	200	15
Polyimide film (PI)	-92.88	400	250
Duralar polyester film (PET)	-89.44	150	80
Polyvinylidene fluoride (PVDF)	-87.35	150	60
Polyetheretherketone (PEEK)	-76.25	240	100
Polyethylene (PE)	-71.2	80	30
High-temperature silicone rubber	-69.95	250	15
Wear-resistant garolite	-68.51	120	140
Low-density polyethylene (LDPE)	-67.94	80	15
High impact polystyrene (PS)	-67.37	70	40
High-density polyethylene (HDPE)	-59.91	80	30
Weather-resistant EPDM rubber	-53.61	150	20
Leather strip (Smooth)	-52.75	65	30
Oil-filled cast nylon 6 (PA-6)	-49.59	80	80
Clear cast acrylic (PMMA)	-48.73	70	80
Silicone	-47.3	230	15
Abrasion-resistant SBR rubber	-40.13	100	28
Flexible leather strip (Smooth)	-34.4	65	30
Noryl polyphenyl ether	-31.82	120	80
Poly(phenylene sulfide) (PPS)	-31.82	200	100
Pigskin (Smooth)	-30.1	65	30
Polypropylene (PP)	-27.23	100	50
Slippery nylon 66 (PA-66)	-26.09	150	110
Weather- and chemical-resistant santoprene rubber	-25.23	125	20
Chemical- and steam-resistant aflas rubber	-22.65	200	30
Polysulfone	-18.92	150	80
Cast nylon 6 (PA-6)	-18.35	80	80
Copy paper	-18.35	250	25
Chemical-resistant and low-temperature fluorosilicone rubber	-18.06	230	15
Delrin® acetal resin	-14.91	90	80
Wood (Marine-grade Plywood)	-14.05	25	110
Wear-resistant slippery garolite	-11.47	120	140
Super-stretchable and abrasion-resistant natural rubber	-10.61	70	40
Oil-resistant buna-N rubber	2.49	100	30
Food-grade oil-resistant buna-N/Vinyl rubber	2.95	100	30

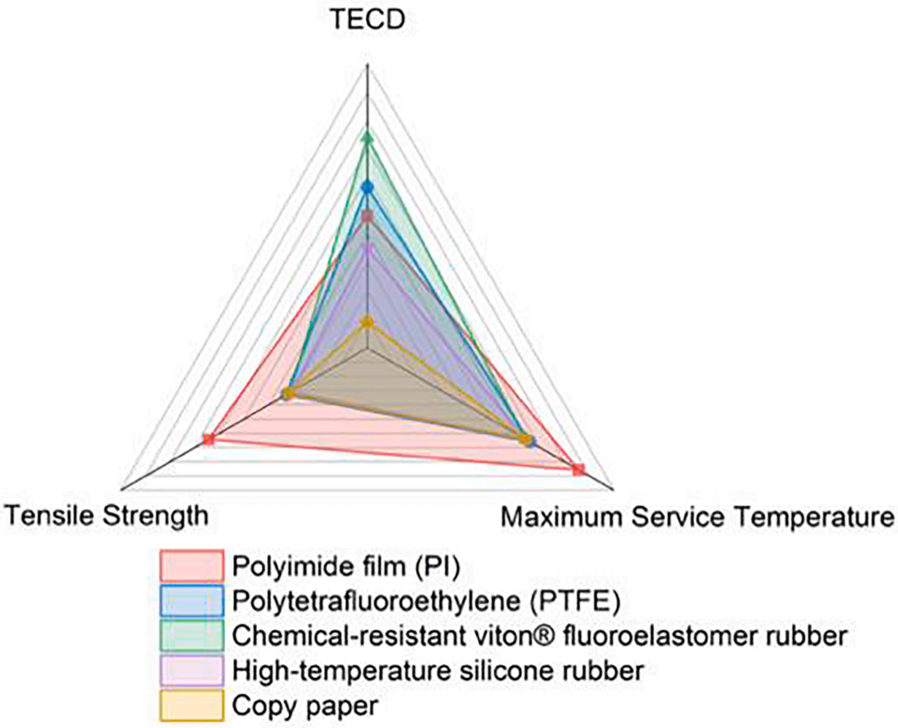

Fig. 1. The comparison of five HT resistant materials.

select the appropriate materials for different environments. For example, in HT and high-stress environments, PI is likely to stand out and become the optimal choice of material. Alternatively, if you only require the triboelectric material to maintain good mechanical strength at room temperature, then Garolite G-10 would be the preferred choice. The Fig. 1 illustrates the proportion of three performance metrics for five HT materials

Although early studies found that PI has weaker piezoelectric properties, it exhibits excellent piezoelectric response at HTs, which the piezoelectric coefficient d_{31} of 3,3′-diaminodiphenylsulfone (DDS) /4,4′-oxydiphthalic anhydride (ODPA) PI was 30 pC/N at 200℃ compare with it at room temperature, in which the d_{31} was 0.2 pC/N at 25℃ [60,61], resulting in its undesirable mechanical–electrical energy conversion efficiency. Ordinary PIs are rarely used as piezoelectric materials for the PENG. However, due to its excellent physical and chemical properties, electrical characteristics, as well as market share, it has incomparable advantages in the application of flexible nanogenerator materials. It would be very meaningful to study the application of PI materials in the field of energy harvesting.

To investigate the working mechanism of the power generation of PI nanofibers, a novel method of fast Fourier transform (FFT) has been implemented for output signal analysing [62] and decoupling purposes. In this regard decoupling piezoelectric and triboelectric signals from the synthesized membrane has been performed using the FFT. The discovery holds immense potential for the development of the next generation of PENG and TENG devices with highly accurate electrical outputs.

KPFM measurement confirmed the positive surface potential of PI nanofibers due to the high voltage electrospinning. In addition, the energy conversion performance exhibits an interesting behavior in rising temperature environments, increasing at early stage of elevation and decreasing with a further elevation once reaching the highest level around 160 ℃. Theoretical studies have been conducted to explore the interaction between the CE and TE in multi-temperature layers nanogenerators, addressing this scientific gap.

2. Materials

Para-phenylenediamine (PDA) is used as the diamine, with 98 % purity. 4,4′-oxydiphthalic anhydride (ODPA) was used as the dianhydride, with 97 % purity. N, N-dimethylacetamide (DMAc, 99 %) is the suitable solvent for the synthesis. All the chemicals were purchased from Sigma-Aldrich (Australia) and used as supplied. Commercial piezoelectric (PE) polyvinylidene difluoride (PVDF, 28 μm;) was purchased from PolyK Technologies, USA.

3. Experimental

3.1. *PAA solution preparation*

The PI can be obtained in two steps. The PAA was prepared by the monomer ODPA and PDA as the precursor for PI. In detail, 0.005 mol each of ODPA and PDA was dissolved in an equal volume of DMAc separately to obtain the same molarity solutions. Then added the PDA solution into the ODPA solution with vigorous mechanical stirring using a magnetic stirrer at room temperature to form homogeneous precursors. Five concentrations from 16 wt% to 20 wt% of PAA solutions were prepared.

3.2. *Electrospinning and imidization*

A needle-based electrospinning setup was employed to prepare the PAA nanofiber membrane. During electrospinning, the applied voltage, flow rate of the PAA solution, and electrospinning distance were controlled at 15 kV, 0.6 mL h^{-1}, and 15 cm, respectively. The collector was a grounded steel drum (length, 11 cm; diameter, 5 cm). The thickness of the membrane was controlled by the fabrication time (1–5 h). The PAA nanofiber membranes were imidized (Fig. 2(I)) in the oven with the following procedure: 100 ℃ for 1 h, 200 ℃ for 1 h, and 300 ℃ for 1 h.

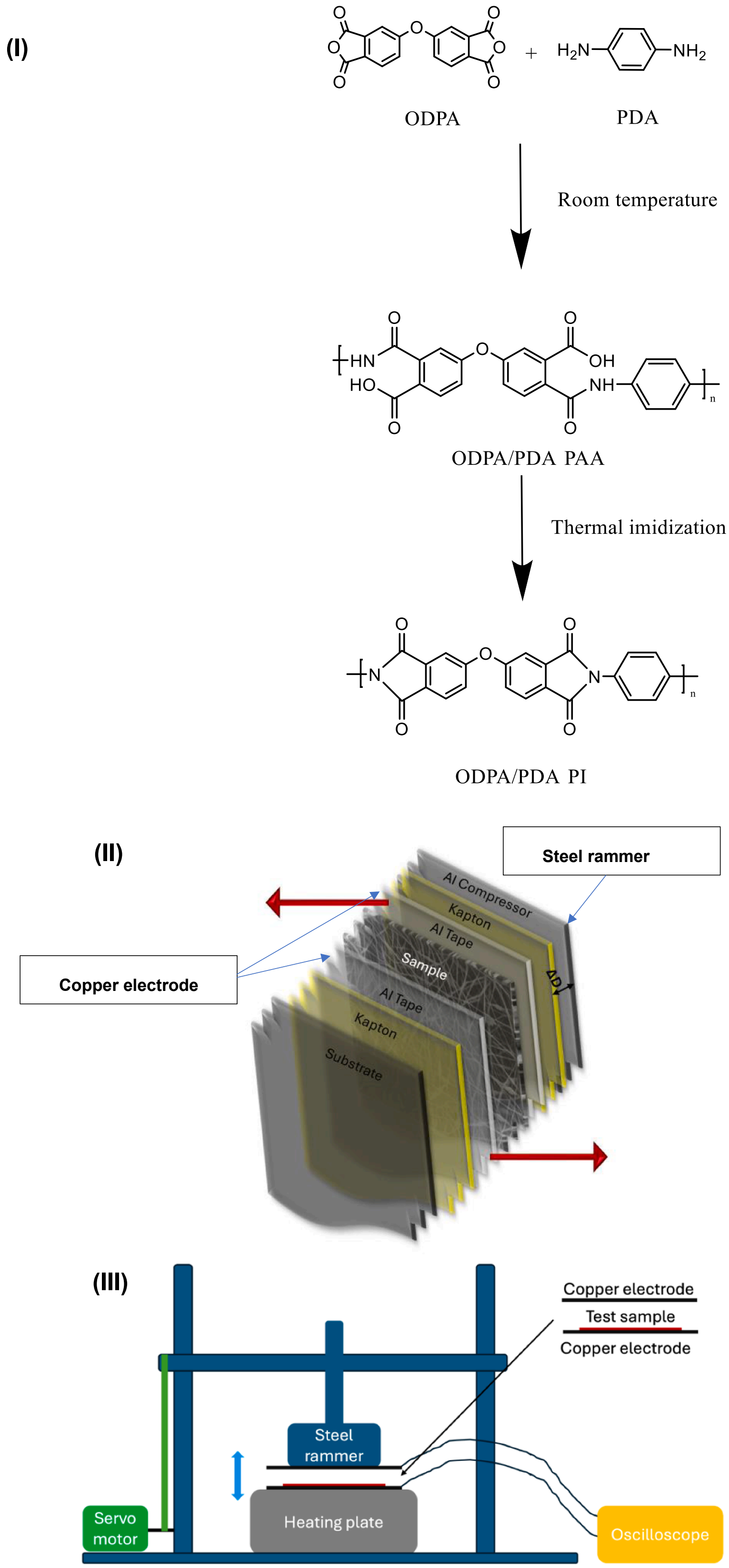

Fig. 2. (I) A schematic of the thermal imidazation process; (II) Schematic of the TENG utilized for signal analysis and electromechanical characterization. (III) Schematic diagram of the self-designed testing platform for triboelectric performance. (IV) Viscosity of different concentrations of dope by shear rate(a); Electrospun PI membranes and their SEM images (b); FTIR spectra of the PAA membranes (c); FTIR spectra of the PI membranes (d); and Comparison between the PAA and PI FTIR spectra(e); (V)SEM images of (a-e) electrospun PI nanofiber membranes.

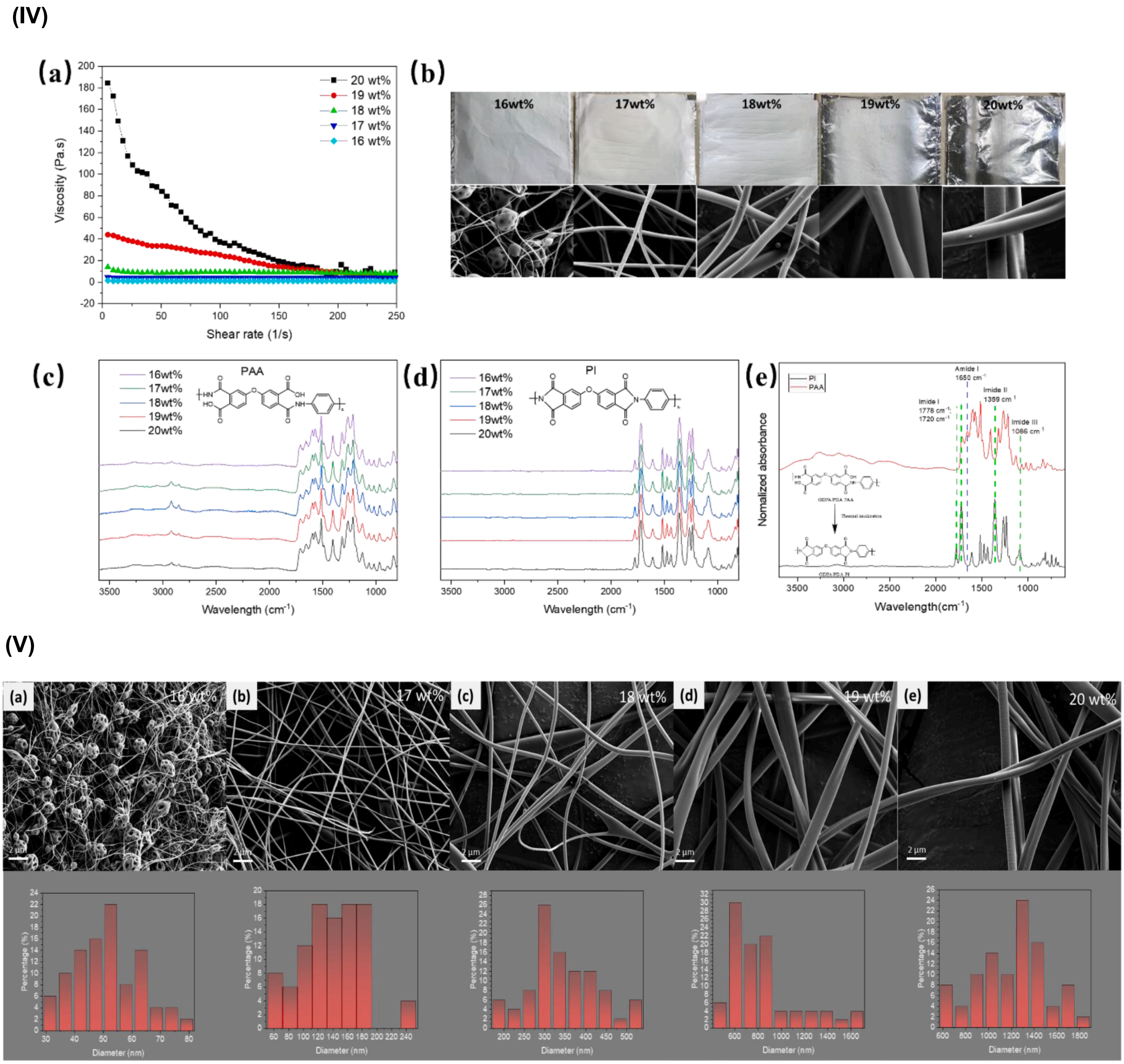

Fig. 2. (*continued*).

3.3. Preparation of the samples for the energy conversion test

Both the PAA and PI membranes are prepared by sandwiching one layer of nanofiber membrane with two aluminum foils of electrodes (thickness 20 μm). The sample was covered by one layer of PI tape (thickness 80 μm) both on top and bottom sides.

3.4. Characterization techniques

To investigate the effect of the electrospinning technique, imidization and heat treatment on PI energy conversion performance, several characterization techniques were utilized: Nanofiber morphology and diameter are investigated and measured using scanning electron microscopy (SEM, Zeiss Supra 55VP). The thickness of the nanofiber membrane was measured using a digital micrometer. Differential scanning calorimetry (DSC, TA Q200) and thermogravimetric analysis (TGA, Netzsch) was used to characterize the temperature resistance properties of the PI nanofiber samples. The rheology of the PAA solutions was measured using dynamic mechanical analysis (DMA) test (TA HR Rheometer). The chemical structure transformation of the materials was observed by Fourier transform infrared spectroscopy, attenuated total reflectance (ATR) mode. (FTIR, Bruker Vertex 70). Voltage outputs were recorded on an oscilloscope (Rohde & Schwarz, RTM3004) with a compression force of 10 N with working areas of 4 cm^{-2} and a frequency of 2 Hz.

3.5. Signal decoupling

3.5.1. Testing and electrical measurement

As illustrated in Fig. 2(III), a force of 15 N, a contact area of 4 cm^{-2}, with a pre-load of 5 N, was applied on an aluminium compressor at a frequency of 0.5 Hz for ramp mode and 5 Hz for sine mode during the contact separation mode testing of nanogenerator sensors. The displacement (ΔD) between the aluminium compressor and the sample was maintained at 0.044 mm, with a dwell time of 1 s for each cycle of the ramp mode. Signal extraction was performed following 60 cycles of 15 N force. Current signals were recorded using a pre-amplifier (SR570, Stanford Research Systems, USA) and an oscilloscope (TDS 1012B, Tektronix, USA).

Table 2

Zero-shear viscosity of PAA dope and their corresponding electrospun PI fiber diameter.

Concentrations	16 wt%	17 wt%	18 wt%	19 wt%	20 wt%
Zero shear viscosity (Pa*s)	1.51	4.53	13.88	43.94	184.58
Fiber diameter (nm)	53.76	148.59	361.05	895.60	1271.70

3.5.2. Fast Fourier transform (FFT)

FFT was executed in silico using DAQExpress (v5.1) software with the application of the Hanning windowing function. Subsequent data processing, including the extraction of the root mean square (RMS) value and normalization between 0 and 1, was performed using MATLAB (R2022A) and OriginLab (2022b). The frequency axis of the spectra was constrained below 50 Hz, while maintaining the original spectrum length at 500 Hz (Nyquist limit), aligned with the 1000 Hz sampling rate.

3.6. Energy harvesting performance measurements

The triboelectric performance of the sample was tested using a self-designed platform, as shown in the Fig. 2(III). A 2*2 cm sample was placed on a copper electrode sheet on the heating plate, which could adjust the temperature from room temperature to 300 °C. The 1 kg steel rammer was connected to another copper electrode and driven by a servo motor. By programming the servo motor, different movement modes of the steel rammer, such as varying frequencies and displacements, could be achieved. In this study, the testing frequency was set to 2 Hz, with a displacement of 3 mm in tapping mode, meaning a force of 9.8 N was applied to the sample for each tap during the test. The voltage output was measured using an oscilloscope. To minimize the impact of humidity and temperature fluctuations, all comparative samples were tested on the same day in a continuous manner. The room temperature is 20 °C as the tests were conducted in a temperature-controlled lab with the temperature maintained at 20 °C.

3.7. KPFM

The surface potential or contact potential difference (CPD) of the requisite PI fibers were measured in this study with the KPFM technique using a Bruker, Dimension Edge^{TM} Atomic Force Microscope (AFM). All the surface potential measurements in this study were carried out at ambient (lab) temperature, pressure and humidity conditions using the enclosure provided by the manufacturer of the equipment. The CPD was studied over the scan areas of (1 * 1 μm^2) and (5 * 5 μm^2). In this technique the surface potential distribution was estimated by applying an AC voltage and plus a DC voltage to the AFM tip. The appropriate electrical conductivity between the tip, sample and AFM holder was ensured, as the fibers were coated on aluminum substrate.

The surface potential or contact potential difference between the tip and sample were determined simultaneously with the topographical measurement, both the data were procured at same pixel density of 256 * 256 pixels per image and a scan rate of 0.8 $\mu m\ s^{-1}$ for 1 * 1 μm^2 image area and scan rate of 2 $\mu m\ s^{-1}$ for 5 * 5 μm^2 image area. Here, an antimony (n) doped silicon tip (SCM-PIT-V_2, Bruker) with a radius of 25 nm was used. The tip was coated on both back and front sides with platinum-iridium (Pt-Ir) material, to laterally resolve the surface potential distribution of PI fibers. This tip was supported on an antimony (n) doped silicon cantilever with thickness of 2.8 μm coated only on the backside with Pt-Ir material, possessed with a resistivity of 0.01–0.025 Ω cm. Both the AFM and surface potential data obtained were analyzed with Gwyddion software. The high frequency associated with KPFM images were processed with a low pass filter.

Table 3

Characteristic FTIR peaks for PI and PAA.

Group	Frequency (cm^{-1})	Mode
Imide I	1770–1780;1720–1740	C=O stretching
Imide II	1360–1380	C-N stretching
Imide III	1070–1090	C-H bending
Amide I	1650	C=O (CONH) stretching

Table 4

The V_{OC} output of electrospun PI membranes with different dope concentrations and viscosities.

Item	Dope concentration (wt %)	The zero-shear viscosity (Pa*s)	Output (V_{OC})
PI-16	16	1.12	1.71
PI-17	17	2.24	4.67
PI-18	18	6.27	5.98
PI-19	19	21.32	1.84
PI-20	20	184.58	1.96

4. Result and discussions

4.1. Physicochemical properties and surface morphology of nanofiber membranes

PAA nanofiber membranes at concentrations ranging from 16 wt% to 20 wt% for subsequent imidization. The zero-shear viscosity of the PAA solutions was examined, revealing an increase from 1.51 Pa*s to 184.58 Pa*s with varying dope concentrations. This viscosity index increased exponentially with concentration. (see Table 2).

To examine the structural properties of the nanofibers, SEM imaging was employed, as depicted in Fig. 2(V) (a-e). An increase in average diameter of the electrospun PI fibers from 53.76 nm (16 wt%) to 1271.70 nm (20 wt%) with rising dope solution viscosity is observed. Serious defects were observed in the nanofiber mats produced from the 16 wt% concentration solution. Nanofibers were successfully electrospun at concentrations below 19 wt%, achieving nanoscale dimensions.

FTIR was employed as a practical tool to monitor the imidization process from PAA to PI. The FTIR spectra of PAA, as illustrated in Fig. 2 (IV) (c-e), displays characteristic peaks, including the N–H stretch (2900–3200 cm^{-1}), the C=O carbonyl stretch from carboxylic acid (1720 cm^{-1}), and the C=O carbonyl stretch from the amide (1650 cm^{-1} or amide I band). After imidization treatment, the disappearance of the amide I band at 1650 cm^{-1} indicates the transformation from PAA to PI (Fig. 2(IV) (c-e)). characteristic peaks at 1778 cm^{-1} (Imide I), 1360 cm^{-1} (Imide II), and 1087 cm^{-1} (Imide III) emerge, confirming the successful imidization. The FTIR analysis is shown in Table 3.

4.2. Energy conversion performance

4.2.1. V_{OC} and charging ability

By controlling the electrospinning time, PI-18 membranes of varying thicknesses from 15 μm to 134 μm were obtained. As the thickness of the nanofiber membrane increased, a corresponding enhancement in the sample's output capability was observed. This can be explained that the increased thickness of the membrane can be attributed to a larger surface area, indicating a higher capability for the accumulation of surface charges

The zero-shear viscosity of the dope solution plays a crucial role in the electrospinning process, determining the formation of a suitable nano-scale fibrous membrane. The concentration of the dope solution

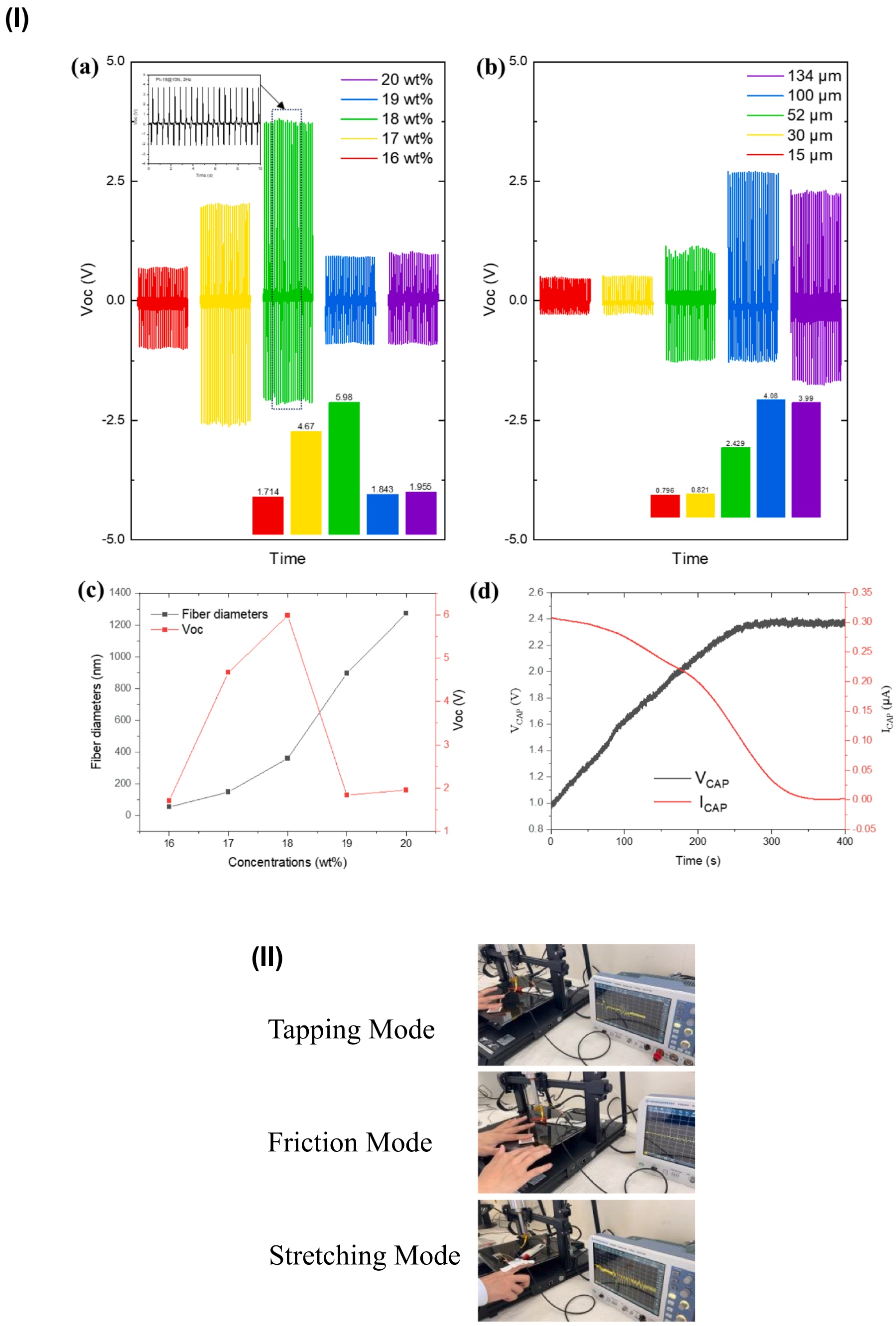

Fig. 3. (I) V_{OC} output of different concentrations of electropun PI membranes (a); V_{OC} output with different electropun PI membrane thicknesses (b); V_{OC} and fiber diameters with concentrations from 16 wt%-20 wt% (c); Charging performance of PI-18 membranes (d) and; (II)Signal generation of electropun PI membranes with different real working modes; (III) Current signal of PVDF film with ramp mode (a); Current signal of PI-18 with ramp mode (b); Current signal of a PVDF film and PI-18 with sine mode (c); The FFT result of the current signal of the PVDF film and PI-18 with sine mode (d-e).(IV) KPFM measurement of electrospun PI nanofibers; Height and V_{SP} images of nanofibers deposited on aluminium foil at a scanning area of 1 μm^2 (a) and 5 μm^2 (b) and; (V)Schematic depicting the formation of surface charge on the fibers during the electrospinning process (c).

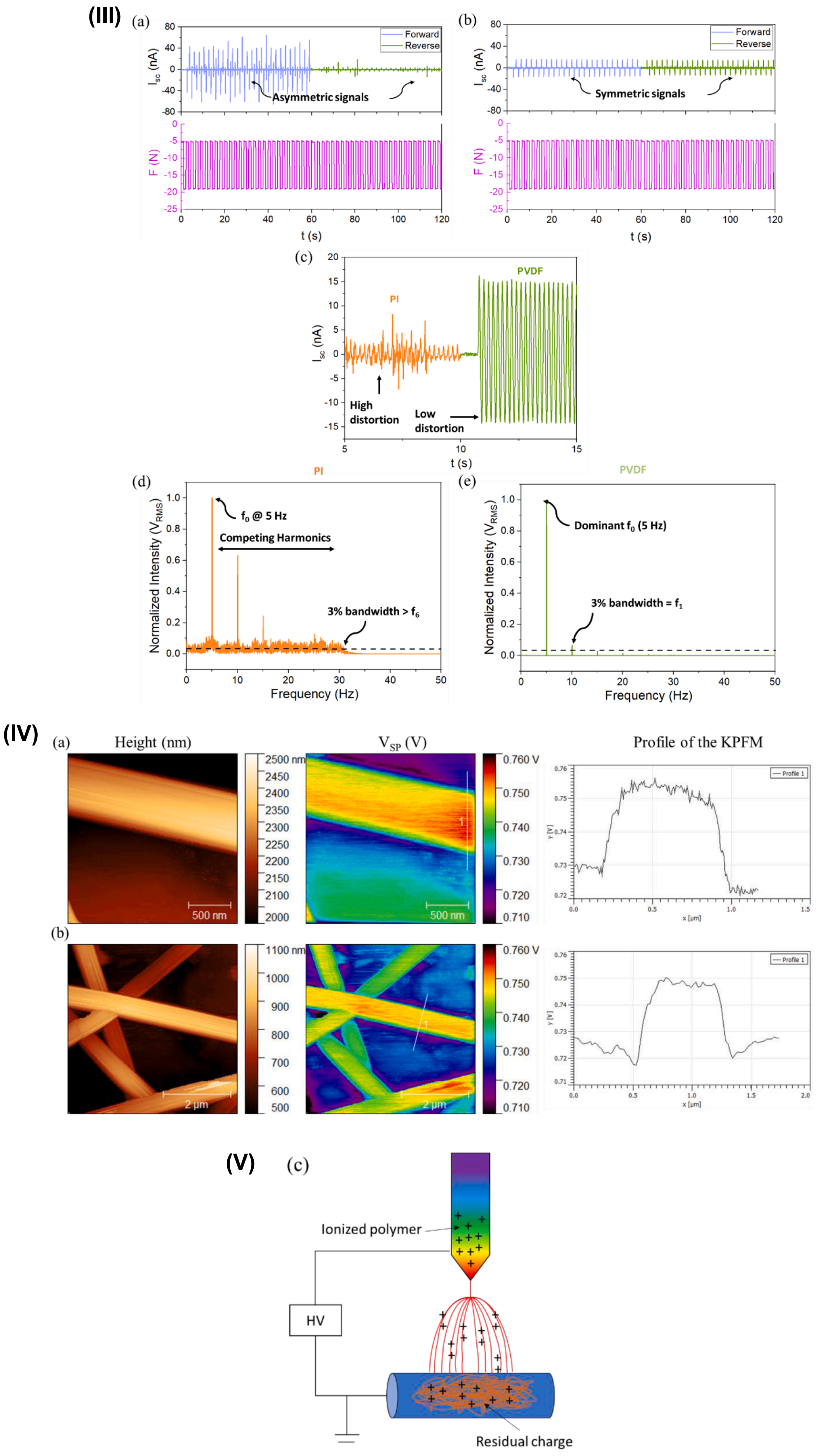

Fig. 3. (*continued*).

Table 5
The frequency domain properties of the output signal.

Item	Testing configuration	f_o (Hz)	f_{max} (Hz)	f_r
PVDF film [62]	Contact mode	3	9	3
PI film [62]	Contact mode	3	15	5
PVDF film (this work)	Contact mode	5	10	2
PI-18 (this work)	Contact mode	5	30	6

was varied from 16 wt% to 20 wt%, leading to a substantial increase in zero-shear viscosity from 1.12 Pa*s to 184.58 Pa*s. (see Table 4).The resulting output performance of PI nanofiber membranes (100 μm) was analyzed. Among the concentrations tested, the peak-to-peak V_{OC} output of the PI nanofiber membrane demonstrated a rising trend, starting from 1.71 V at 16 wt% and peaking at 5.98 V at 18 wt% (PI-18). However, a decline in output performance was observed at higher concentrations of 19 wt% and 20 wt%, suggesting that the 18 wt% PAA dope, possessing a viscosity of 6.27 Pa*s, emerged as the most suitable concentration for PI electrospinning in case of energy conversion applications. The PI-18 was examined by charging ability in this paper. The generated charges were stored using a rectifier and a storage device, connecting capacitors in parallel. The voltage across a single capacitor of 47 μF, was monitored during the charging process. It began at 0.98 V and reached 2.38 V within 360 s, as illustrated in Fig. 3(I) d, the corresponding charge ability can be calculated by the equations (1)–(3). The maximum charging current can reach to 0.30 μA.

$$Q_{CAP} = C \times V_{CAP} \tag{1}$$

$$Q_{CAP} = \int_0^t I_{CAP} dt \tag{2}$$

$$I_{CAP} = \frac{dQ_{CAP}}{dt} = C\frac{dV_{CAP}}{dt} \tag{3}$$

where Q_{CAP} denotes the charge stored in the capacitor, C denotes the capacitance, I_{CAP} denotes the current charged into the capacitor, and V_{CAP} denotes the voltage of the capacitor.

Additionally, PI-18 can generate voltage level V_{OC} signals under different working modes such as friction, stretching, and tapping, as shown in Fig. 3(II). This presents promising applications in high-performance sensor development.

4.3. Signal identification

Triboelectric and piezoelectric generation are the most common mechanisms in material-based power generator. The energy conversion performance observed may contribute from either of these mechanisms individually or a combination of both. Identifying their working mechanisms plays a crucial role in subsequent theoretical research and improving material performance.

4.3.1. FFT methods

To investigate the output signal characteristics of electrospun PI nanofibers, we employed a PVDF film as a reference for comparative analysis. Forward and reverse connections were two different connection configurations when the positive and negative probes of the ammeter were interchanged. For piezoelectric signals, this should not make a significant difference, since the polarisation of the material produces an electrical potential that would invert when interchanged but the intensities of the signals should remain the same.

In the ramp mode test of the PVDF film, as illustrated in Fig. 3(III) b, both forward and reverse directions exhibited symmetrical signal characteristics. However, in the case of PI-18 (Fig. 3(III) (a), a stronger current output signal was detected in the forward direction, while it was relatively weaker in the reverse direction, revealing asymmetrical signal characteristics. This result can be attributed to the fact that the PI sample lacks piezoelectric performance. Since piezoelectric properties are caused by the deformation of materials leading to changes in electrical performance, the test surface of the sample does not show selectivity. If the sample demonstrates selectivity on the test surface, it further indicates that it does not exhibit significant piezoelectric properties.

When the compressor was subjected to a sine wave input instead of the previous ramp input, no dwell period was introduced between each compression and retraction phase, leading to continuous displacement. In this case, a weaker signal was observed in the PI-18, illustrated in Fig. 3(III) (c), potentially indicating charge loss due to destructive interference of polarization. However, in the case of the PVDF film, where polarization is highly directive, a substantially larger signal was observed. And the intensity of the signal remained consistent with the previous input scenario. To analyze the difference in these V_{OC} signals, FFT was performed to convert the V_{OC} data from the time domain to the frequency domain (Fig. 3(III) (d-e)). PVDF film shows a piezoelectric signal with a bandwidth (f_{max}), which is determined by the intensity of a harmonic less than 3 % of the intensity of the fundamental frequency (f_0 = 5 Hz), of 10 Hz compared to the PI-18 signal with a wide range competing harmonic bandwidth at 30 Hz. This result is close to the previous work on PI film as the bandwidth was found at 15 Hz in case of 3 Hz fundamental frequency [62].

To compare signals with different fundamental frequencies, we introduced a relative bandwidth ratio f_r, calcuted as $f_r = \frac{f_{max}}{f_0}$, to characterize the intensity of competing harmonic signals. A higher f_r indicates a higher distortion signal. Under the contact mode measurement, as shown in Table 5, the f_r of PI is 5 for the film and 6 for the electrospun nanofibers, compared to f_r of 2–3 for piezoelectric, exhibiting highly distinctive triboelectric signal characteristics.

These changes exhibit a certain consistency across the entire fiber membrane, making it not easily observable in the time-domain signal. Transforming the signal into the frequency domain through FFT allows for a more intuitive observation of these signal features.

4.3.2. KPFM measurement

KPFM is a technique for nanoscale surface potential measurement, capable of illustrating variations in the surface potential voltage (V_{SP}) of materials. Fig. 3 (IV and V) respectively, depict the KPFM scans conducted on electrospun PI fibers on an aluminium foil surface, at scales of 2 μm and 5 μm. The height map displays the nanoscale morphology of the fibers. The V_{SP} map revealed that the V_{SP} of the PI fibers is higher than that of the aluminium foil surface. After conducting profile analysis of the fiber surface, it was observed that the voltage ranges from 750 mV to 755 mV, with a concentration of higher V_{SP} in the middle area of the fibers. This is attributed to the electrospinning process of the PI nanofibers conducted at a high positive voltage (15 kV), resulting in the polymer solution ionized and residual charges embedded on nanofibers surface once collected by aluminium foil [63], as illustrated in Fig. 3(V), thus exhibiting higher positive V_{SP}. Surfaces with higher V_{SP} are more prone to electron accumulation during contact with positive materials, hence demonstrating stronger electronegative property. This also explains the excellent power generation performance of the electrospun PI fibers as a negative dielectric material. To the best of our knowledge, this is the first reported KPFM study, specifically targeting nanoscale electrospun PI fibers. (Fig. 3(IV and V).

4.4. High temperature performance

The optimal sample PI-18 (100 μm) and its corresponding pre-product PAA-18 were picked for the temperature resistance study. Based on the DSC curves of electrospun PAA and electrospun PI, as shown in Fig. 4I, the glass transition temperature (T_g) of PAA-18 was determined to be 188 ℃, while the T_g of the PI-18 was found to be 315 ℃. Comparing the T_g of PI-18 (315 ℃) with the T_g of the bulk ODPA/PDA PI (326 ℃) [64], it can be confirmed that the PI nanofiber

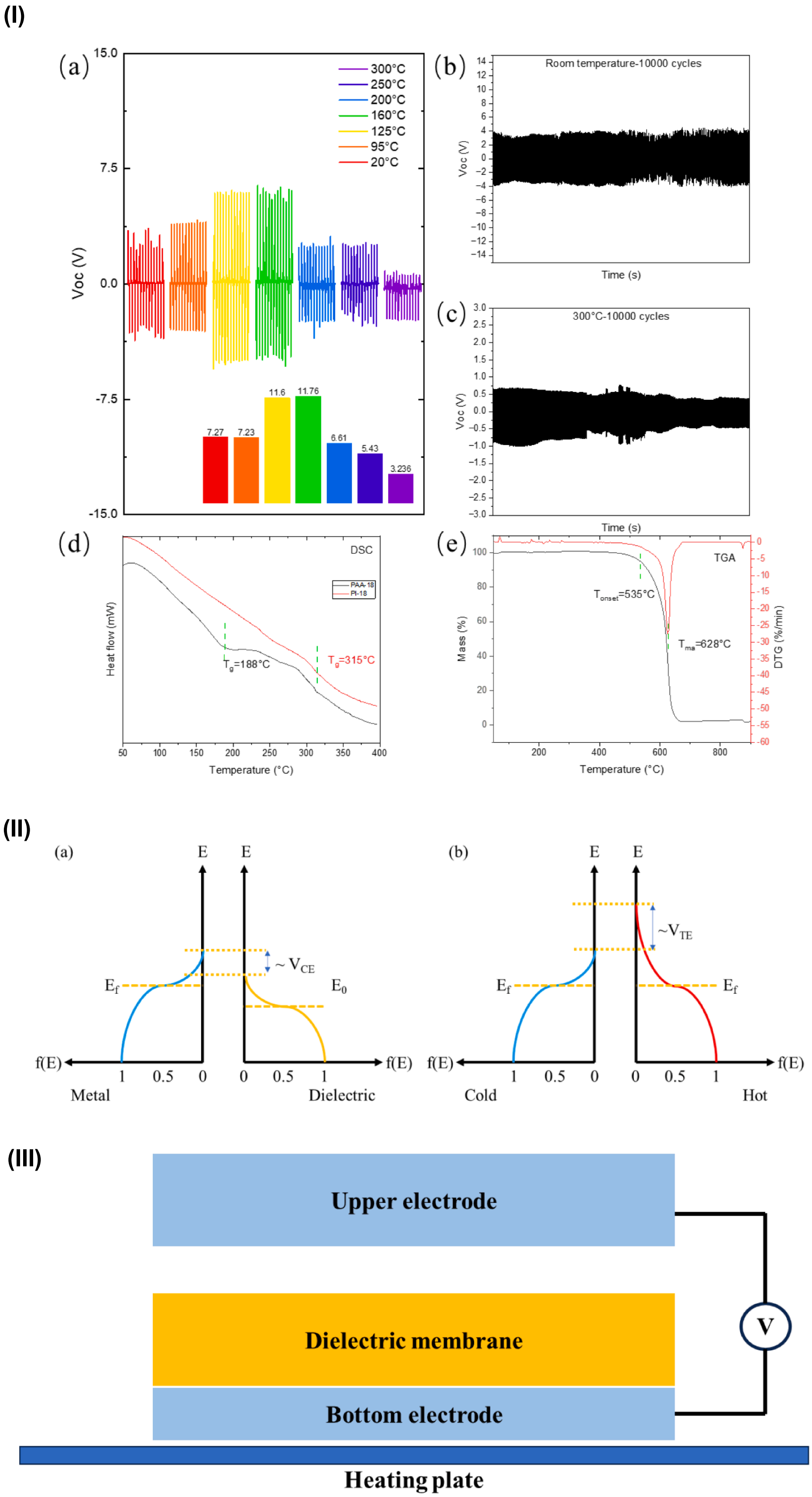

Fig. 4. (I) V_{OC} output of the PI-18 with elevated temperature (a); Durability test (10000 cycles) of V_{OC} output for PI-18 at room temperature (b); Durability test (10000 cycles) of V_{OC} output for PI-18 at 300 oC (c); DSC curves of electrospun PAA and electrospun PI (d) and; TGA and DTG curves of PI (e); (II) The band structure of the metal and the dielectric when the Ef of the metal is higher than the highest occupied surface state level (E0) of the dielectric, the energy difference is approximately contact electrification voltage, such that VCE (a). The band structure when the same materials with different temperatures, the energy difference is

approximately thermoelectric voltage, such that VTE (b). (III) Schematic of the structure of the TENG used for the high-temperature output testing. (IV). Schematic of the working mechanism of the TENG at room temperature.; (V) The schematic of working mechanism of the TENG at initial-elevated temperature. (VI). The schematic of working mechanism of the TENG at post-elevated temperature.

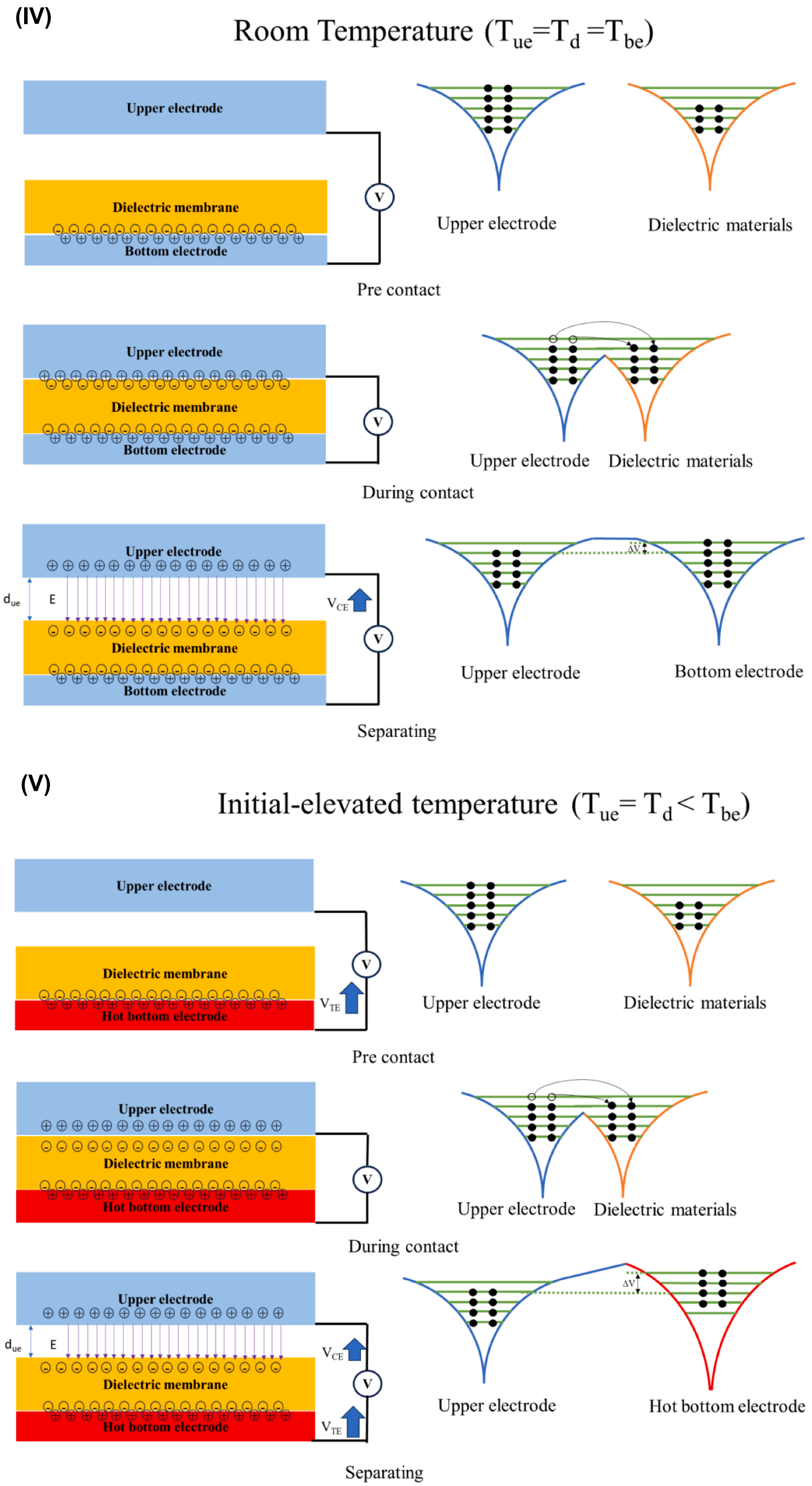

Fig. 4. (*continued*).

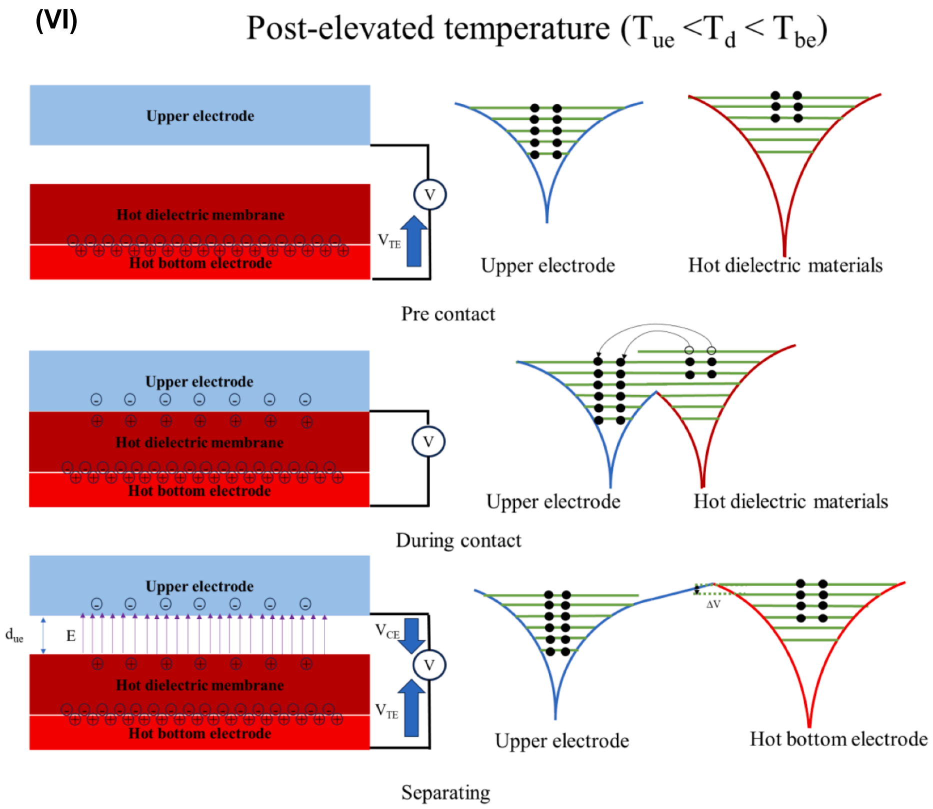

Fig. 4. (*continued*).

membrane still maintained a reasonable level of thermal resistance compared to its conventional film counterpart.

The TGA analysis provides valuable information about the thermal stability and decomposition behaviour of the materials. As illustrated in Fig. 4I(e), the PI-18 exhibited a weight loss of 1 % at 400 ℃. The decomposition of PI-18 begins at around 500 ℃, which is associated with the breakage of the carbonyl functional groups [65]. The T_{onset}, representing the temperature at which 5 % weight loss occurs, was determined to be 535 °C. The T_{ma}, corresponding to the maximum temperature in the derivative of the TGA curve, was around 628 ℃. Additionally, the residual weight at a final temperature of 900 ℃ was 1.9 %. The thermal resistance of the electrospun PI nanofiber membrane, evidenced by these results, makes it a promising material for applications in high-temperature environments.

Table 6

V_{OC} output performance of polymer nanogenerators with different materials.

	V_{OC}(V)	Maximum working temperature	Ref.
PVDF film	7.02	80 ℃	[69]
PVDF film	10	80 ℃	[70]
PVDF film	98 V	80 ℃	[71]
PVDF film	190 V	80 ℃	[72]
PVDF film	21 V	80 ℃	[73]
PAN nanofibers	9.7	450 ℃	[46]
PDMS film	30 V	200 ℃	[74]
PDMS film	22.3 V	200 ℃	[75]
PDMS film	15 V	200 ℃	[76]
PDMS film	75 V	200 ℃	[77]
PVA film	29.6 V	200 ℃	[78]
PI film (Kapton)	1.18	250 ℃	[57]
PI film (Kapton)	1.8 V	250 ℃	[79]
PI nanofibers	11.76	350 ℃	This work

4.4.1. *High temperature energy conversion*

The high temperature output performance of the PI-18 demonstrated an interesting trend (Fig. 4I(c)), showing an increase with the testing temperature, reaching its highest output of 11.76 V at 160 ℃, and decreasing with a further rise in temperature. However, recent studies on high-temperature TENGs have shown that their output performance tends to decrease as the ambient temperature increases, which is attributed to the thermionic effect on the dielectric surface [66–68]. In contrast, our experimental results indicate that in multilayer structures, the varying temperature transmission across layers creates a relative temperature gradient, leading to an unusual impact on the TENG's output performance. This can be explained by the competition between decreased contact electrification (CE) and increased thermoelectric effect (TE) [66]. According to Fermi–Dirac statistics, the density of excited electrons can be expressed by equation:

$$f(E) = \frac{1}{e^{(E-E_f)/kT} + 1} \tag{4}$$

where f(E) is the occupation probability of a state of energy E, k is Boltzmann's constant, E_f is the Fermi level of the material, and T is the temperature in Kelvin.

According to Equation (4), electrons within materials at elevated temperatures occupy higher energy levels compared to those at lower temperatures. As a result, they tend to migrate from the hotter side to the colder side, leading to a detectable thermoelectric voltage difference (V_{TE}). V_{TE} can be calculated as:

$$V_{TE} = \int_{T_{ue}}^{T_{be}} S(T)dT \tag{5}$$

where the S(T) denotes the Seebeck coefficient, which is a function of temperature, T_{be} denotes the temperature of bottom electrode, and T_{ue} denotes the temperature of upper electrode.

While the V_{OC} contributed by contact electrification can be calculated as V_{CE}.

$$V_{CE} = \frac{-\sigma \bullet d}{\varepsilon_0} \tag{6}$$

where σ denotes the surface charge density, d denotes the displacement between electrode and dielectric, ε_0 denotes the vacuum dielectric constant.

Surface charge density plays a key role in term of V_{CE} output, it can be expressed by equation [68]:

$$\sigma = -e\int_{E_0+kT_d}^{E_f+kT_{ue}} N(E)dE \tag{7}$$

where e denotes the elementary charge, $N(E)$ denotes the surface state density of the dielectric, T_d denotes the temperature of dielectric material.

Therefore, we can establish the relationship between V_{OC} and the temperatures of the dielectric and electrodes with equation:

$$\mathrm{VOC} = \mathrm{VCE} + \mathrm{VTE} = \frac{d \bullet e}{\varepsilon_0}\int_{E_0+kT_d}^{E_f+kT_{ue}} N(E)dE + \int_{T_{ue}}^{T_{be}} S(T)dT \tag{8}$$

In this study, the structure of the TENG used for high-temperature output testing is shown in the Fig. 4(III). It consists of two layers of aluminium electrodes, with a layer of PI nanofiber dielectric material in between that was prepared in-house. The lower electrode contacts with the heating plate, and as the heating plate continuously heats up, the lower electrode and the PI nanofiber are heated. The upper electrode, due to its continuous motion, does not remain in continuous contact with the heat source, resulting in its temperature remaining lower than that of the dielectric layer and lower electrode throughout the testing process. Therefore, the testing can be divided into three stages for discussion, corresponding to different temperature conditions: (1) room temperature, (2) initial-elevated temperature and (3) post-elevated temperature.

At room temperature, there is no difference between the temperatures of the upper electrode (T_{ue}), bottom electrode (T_{be}), and dielectric membrane (T_d), where $T_{ue} = T_d = T_{be}$. When the dielectric membrane contacts with the upper electrode, its surface accumulates a certain amount of charge, thereby generating V_{CE} output. Meanwhile, due to the absence of temperature disparities between the upper and lower electrodes, no TE occurs. According to equation (8), we can also calculate that V_{TE} equals to zero when $T_{ue} = T_{be}$. The V_{OC} output strength was only determined by the upper electrode's E_f and dielectric membrane's E_0 at a certain measurement condition. The working mechanism of this scenario is shown in Fig. 4(IV). Furthermore, under initial-elevated temperatures, the bottom electrode will be heated first due to the heat pad's location beneath it, where $T_{ue} = T_d < T_{be}$. This causes electrons in the bottom electrode to exhibit even higher energy levels, resulting in V_{TE} output compared to the room temperature scenario, as depicted in Fig. 4 (V). According to equation (8), the strength of V_{TE} can be determined by T_{ue} and T_{be}. This leads to an enhancement in the V_{OC} output of the TENG device at initial-elevated temperatures.

Continuing to elevate the temperature, the dielectric membrane will also heat up, and the temperature between each layer can be expressed as $T_{ue} < T_d < T_{be}$. At this stage, electrons in the dielectric membrane become excited and migrate to the upper electrode during contact. According to equation (8), although the V_{TE} increased with further temperature difference, the V_{CE} diminishes as the energy state of the dielectric membrane $E_0 + kT_d$ approaches that of the upper electrode $E_f + kT_{ue}$. Therefore, the disparity in energy levels between the upper and bottom electrodes decreases, weakening the V_{OC} output, as illustrated in Fig. 4(VI).

The output of the nanogenerator exhibited excellent stability, retaining 96.5 % of its original performance after 10,000 cycles at room temperature, shown in Fig. 4. However, in the challenging high-temperature environment of 300 ℃, the retention capability decreased to 56.8 % after the same number of cycles (10,000), shown in Fig. 4 (c). As the duration of high-temperature testing extends, both T_d and T_{ue} gradually increased, and thus the V_{CE} and V_{TE} will simultaneously weaken. Meanwhile, the effect of thermionic emissions should be considered regarding the surface charge decay [67]. However, in the test used in this study, which is continuous contact separation mode, the surface charge of dielectric membranes remains charged during contact with metal, limiting the impact of thermionic emissions on the output performance.

Taking a V_{OC} output performance comparison between the PI nanofibers and recent common polymeric materials, as illustrated in Table 6, Based on the table, the primary advantage of PI nanofibers is their high thermal stability (350 °C), which is significantly superior to most other materials, such as PVDF (80 °C), PDMS (200 °C), and PVA (200 °C). This high-temperature resistance makes PI nanofibers suitable for energy harvesting applications in extreme environments. Additionally, their Voc (11.76 V) is higher than that of Kapton PI films (1.18 V and 1.8 V), suggesting that the nanofiber structure may enhance the PI triboelectricity.

However, PI nanofibers show lower Voc than some high-output materials, such as PDMS (up to 75 V) and PVDF (up to 190 V). One reason could be the inconsistency in testing conditions. Variations in measurement parameters, such as electrode configuration, applied force, frequency, or humidity, can significantly impact the reported voltage values. Therefore, a direct comparison between different materials may not always reflect their true performance differences under identical conditions. Nevertheless, PI nanofibers still require further optimization, such as surface modifications or the incorporation of functional fillers (e.g., GO, CNT, or BTO) to enhance their output performance.

5. Conclusion

In summary, this study aimed to investigate the energy conversion performance of electrospun PI nanofiber membranes. Utilizing an 18 wt % concentration PAA dope with a zero-shear viscosity of 6.27 Pa*s proved to be suitable for fabricating nanofiber membranes via electrospinning. The corresponding PI nanofiber membranes displayed optimal energy conversion performance, achieving a V_{OC} output of 5.98 V. FFT analysis confirmed that the source of the V_{OC} output was primarily triboelectricity rather than piezoelectricity. KPFM measurements verified that the surface potential of the PI nanofibers became positive after electrospinning, enhancing their CE abilities. The glass transition temperature of the PI nanofiber membranes exceeded 350 ℃, indicating excellent thermal resistance. Moreover, the combination of CE and TE effects led to an intriguing behaviour in the energy conversion performance of the PI nanofiber nanogenerator at elevated temperatures. The output increased with increasing temperature, reaching a peak V_{OC} of 11.76 V at 160 ℃, representing an 84.4 % improvement compared to room temperature conditions, before declining with further temperature elevation. Additionally, a theoretical investigation into the operational principles of multi-temperature layers was conducted. With their distinctive electrical characteristics, electrospun PI nanofibers showcase the potential to function as temperature-sensitive smart TENGs, particularly in applications demanding resilience in high-temperature environments. Our future lab work will focus on studying piezoelectric/triboelectric polymers in high-temperature environments and exploring the effects of nanoparticles on nanogenerator performance. Also cross-discipline collaboration will be considered to enhance practical applications and establish standardized testing across a wider temperature range. Incorporating novel materials like liquid metals, nanocarbons, MXENE will attribute to higher output and performance and using recycled polymers will promote sustainability. Additionally, advanced methods like fluorination to boost triboelectric response are planned works.

CRediT authorship contribution statement

Peng Wu: Writing – review & editing, Writing – original draft, Visualization, Validation, Methodology, Investigation, Formal analysis, Conceptualization. **Kamyar Shirvanimoghaddam:** Writing – review & editing, Writing – original draft, Supervision, Project administration, Conceptualization. **Ronald T. Leon:** Writing – review & editing, Methodology, Investigation, Formal analysis, Data curation. **Ir. Prasaanth Ravi Anusuyadevi:** Methodology, Formal analysis. **Peyman Taheri:** Investigation, Formal analysis. **Prasad Gonugunta:** Investigation, Formal analysis. **Amanda V. Ellis:** Writing – review & editing, Methodology, Conceptualization. **Minoo Naebe:** Writing – review & editing, Writing – original draft, Supervision, Resources, Project administration, Funding acquisition.

Declaration of competing interest

The authors declare that they have no known competing financial interests or personal relationships that could have appeared to influence the work reported in this paper.

Acknowledgments

The authors would like to thank the Aikenhead Centre for Medical Discovery (ACMD), St Vincent’s Hospital, Melbourne for the provision of facilities to undertake compression testing.

Appendix A. Supplementary data

Supplementary data to this article can be found online at https://doi.org/10.1016/j.cej.2025.161809.

Data availability

Data will be made available on request.

References

[1] P. Bojek, Renewable Power, 2021 [cited 2022 19/06]; Available from: https://www.iea.org/reports/renewable-power.

[2] I. Jung, et al., Flexible piezoelectric polymer-based energy harvesting system for roadway applications, Appl. Energy 197 (2017) 222–229.

[3] H. Shao, et al., Efficient conversion of sound noise into electric energy using electrospun polyacrylonitrile membranes, Nano Energy 75 (2020).

[4] C.A. Howells, Piezoelectric energy for soldier systems, 2008, Army communications-electronics research development and engineering center….

[5] J. Sullivan, L. Gaines, A review of battery life-cycle analysis: state of knowledge and critical needs, 2010.

[6] M. Shirvanimoghaddam, et al., Towards a green and self-powered Internet of Things using piezoelectric energy harvesting, IEEE Access 7 (2019) 94533–94556.

[7] M.M. Abolhasani, K. Shirvanimoghaddam, M. Naebe, PVDF/graphene composite nanofibers with enhanced piezoelectric performance for development of robust nanogenerators, Compos. Sci. Technol. 138 (2017) 49–56.

[8] L. Lu, et al., Flexible PVDF based piezoelectric nanogenerators, Nano Energy 78 (2020) 105251.

[9] D. Hu, et al., Strategies to achieve high performance piezoelectric nanogenerators, Nano Energy 55 (2019) 288–304.

[10] Z.L. Wang, J. Song, Piezoelectric nanogenerators based on zinc oxide nanowire arrays, Science 312 (5771) (2006) 242–246.

[11] F.-R. Fan, Z.-Q. Tian, Z. Lin Wang, Flexible triboelectric generator, Nano Energy 1 (2) (2012) 328–334.

[12] B. Kumar, S.-W. Kim, Energy harvesting based on semiconducting piezoelectric ZnO nanostructures, Nano Energy 1 (3) (2012) 342–355.

[13] X. Chen, et al., 1.6 V nanogenerator for mechanical energy harvesting using PZT nanofibers, Nano Lett. 10 (6) (2010) 2133–2137.

[14] K.-I. Park, et al., Piezoelectric BaTiO3 thin film nanogenerator on plastic substrates, Nano Lett. 10 (12) (2010) 4939–4943.

[15] D. Mandal, S. Yoon, K.J. Kim, Origin of piezoelectricity in an electrospun poly (vinylidene fluoride-trifluoroethylene) nanofiber web-based nanogenerator and nano-pressure sensor, Macromol. Rapid Commun. 32 (11) (2011) 831–837.

[16] X.M. Pan, et al., A self-powered vibration sensor based on electrospun poly (vinylidene fluoride) nanofibres with enhanced piezoelectric response, Smart Mater. Struct. 25 (10) (2016).

[17] J. Tao, et al., Energy harvesting from wind by a piezoelectric harvester, Eng. Struct. 133 (2017) 74–80.

[18] M. Pozzi, M. Zhu, Characterization of a rotary piezoelectric energy harvester based on plucking excitation for knee-joint wearable applications, Smart Mater. Struct. 21 (5) (2012) 055004.

[19] Y. Yoneda, Dancefloor generates electricity at London’s first eco-disco! 2008 [cited 2022 27/06]; Available from: https://inhabitat.com/green-a-go-go-at-londons-first-eco-disco/.

[20] F.R. Fan, W. Tang, Z.L. Wang, Flexible nanogenerators for energy harvesting and self-powered electronics, Adv. Mater. 28 (22) (2016) 4283–4305.

[21] C.-Y. Liu, A.J. Bard, Electrons on dielectrics and contact electrification, Chem. Phys. Lett. 480 (4–6) (2009) 145–156.

[22] L.S. McCarty, G.M. Whitesides, Electrostatic charging due to separation of ions at interfaces: contact electrification of ionic electrets, Angew. Chem. Int. Ed. 47 (12) (2008) 2188–2207.

[23] J. Lowell, The role of material transfer in contact electrification, J. Phys. D Appl. Phys. 10 (17) (1977) L233.

[24] F. Xi, et al., Universal power management strategy for triboelectric nanogenerator, Nano Energy 37 (2017) 168–176.

[25] X. Fan, et al., Ultrathin, rollable, paper-based triboelectric nanogenerator for acoustic energy harvesting and self-powered sound recording, ACS Nano 9 (4) (2015) 4236–4243.

[26] X. Pu, et al., Ultrastretchable, transparent triboelectric nanogenerator as electronic skin for biomechanical energy harvesting and tactile sensing, Sci. Adv. 3 (5) (2017) e1700015.

[27] L. Xu, et al., Coupled triboelectric nanogenerator networks for efficient water wave energy harvesting, ACS Nano 12 (2) (2018) 1849–1858.

[28] J. Wang, et al., Achieving ultrahigh triboelectric charge density for efficient energy harvesting, Nat. Commun. 8 (1) (2017) 88.

[29] K. Dong, et al., 3D orthogonal woven triboelectric nanogenerator for effective biomechanical energy harvesting and as self-powered active motion sensors, Adv. Mater. 29 (38) (2017) 1702648.

[30] Y. Ma, et al., Self-powered, one-stop, and multifunctional implantable triboelectric active sensor for real-time biomedical monitoring, Nano Lett. 16 (10) (2016) 6042–6051.

[31] Z. Zhou, et al., Wireless self-powered sensor networks driven by triboelectric nanogenerator for in-situ real time survey of environmental monitoring, Nano Energy 53 (2018) 501–507.

[32] D. Liu, et al., Wind-driven self-powered wireless environmental sensors for Internet of Things at long distance, Nano Energy 73 (2020) 104819.

[33] S.C. Mannsfeld, et al., Highly sensitive flexible pressure sensors with microstructured rubber dielectric layers, Nat. Mater. 9 (10) (2010) 859–864.

[34] T. He, et al. Self-powered wireless IoT sensor based on triboelectric textile. in 2020 IEEE 33rd international conference on micro electro mechanical systems (MEMS). 2020. IEEE.

[35] M. Baqeri, et al., Influence of processing conditions on polymorphic behavior, crystallinity, and morphology of electrospun poly(VInylidene fluoride) nanofibers, J. Appl. Polym. Sci. 132 (30) (2015).

[36] N. Minoo, L. Tong, W. Xungai, Carbon Nanotubes Reinforced Electrospun Polymer Nanofibres, in: K. Ashok (Ed.), Nanofibers, IntechOpen, Rijeka, 2010.

[37] M.M. Abolhasani, et al., Towards predicting the piezoelectricity and physiochemical properties of the electrospun P (VDF-TrFE) nanogenrators using an artificial neural network, Polym. Test. 66 (2018) 178–188.

[38] M.M. Abolhasani, et al., Thermodynamic approach to tailor porosity in piezoelectric polymer fibers for application in nanogenerators, Nano Energy 62 (2019) 594–600.

[39] M.M. Abolhasani, et al., Hierarchically structured porous piezoelectric polymer nanofibers for energy harvesting, Adv. Sci. 7 (13) (2020) 2000517.

[40] M.M. Abolhasani, et al., Porous graphene/poly(vinylidene fluoride) nanofibers for pressure sensing, J. Appl. Polym. Sci. 139 (14) (2022) 51907.

[41] V. Ghanooni Ahmadabadi, et al., Structure-rate performance relationship in Si nanoparticles-carbon nanofiber composite as flexible anode for lithium-ion batteries, Electrochim. Acta 330 (2020) 135232.

[42] V. Cauda, et al., Nanoconfinement: an effective way to enhance PVDF piezoelectric properties, ACS Appl. Mater. Interfaces 5 (13) (2013) 6430–6437.

[43] V. Cauda, G. Canavese, S. Stassi, Nanostructured piezoelectric polymers, J. Appl. Polym. Sci. 132 (13) (2015).

[44] M.M. Abolhasani, et al., Porous graphene/poly (vinylidene fluoride) nanofibers for pressure sensing, J. Appl. Polym. Sci. 139 (14) (2022) 51907.

[45] M. Naebe, et al., Effects of MWNT nanofillers on structures and properties of PVA electrospun nanofibres, Nanotechnology 18 (22) (2007) 225605.

[46] W. Wang, et al., High-temperature piezoelectric conversion using thermally stabilized electrospun polyacrylonitrile membranes, J. Mater. Chem. A 9 (36) (2021) 20395–20404.

[47] Y. Sun, et al., Flexible piezoelectric energy harvester/sensor with high voltage output over wide temperature range, Nano Energy 61 (2019) 337–345.

[48] Y. Sheiretov, et al., MWM-array sensors for in situ monitoring of high-temperature components in power plants, IEEE Sens. J. 9 (11) (2009) 1527–1536.

[49] A. Vinogradov, F. Holloway, Electro-mechanical properties of the piezoelectric polymer PVDF, Ferroelectrics 226 (1) (1999) 169–181.

[50] X. Zhang, L. Wu, G.M. Sessler, Energy harvesting from vibration with cross-linked polypropylene piezoelectrets, AIP Adv. 5 (7) (2015) 077185.

[51] W.J. Jackson Jr, Liquid crystal polymers. IV. Liquid crystalline aromatic polyesters, Br. Polym. J. 12 (4) (1980) 154–162.

[52] H.J. Lee, et al., High temperature, high power piezoelectric composite transducers, Sensors 14 (8) (2014) 14526–14552.

[53] J. Yan, et al., Performance enhancements in poly (vinylidene fluoride)-based piezoelectric nanogenerators for efficient energy harvesting, Nano Energy 56 (2019) 662–692.

[54] M. Naebe, et al., Carbon nanotube reinforced rigid-rod polyimide, J. Appl. Polym. Sci. 118 (1) (2010) 359–365.

[55] D.J. Liaw, et al., Advanced polyimide materials: Syntheses, physical properties and applications, Prog. Polym. Sci. 37 (7) (2012) 907–974.

[56] C. Li, P. Wang, D. Zhang, Self-healable, stretchable triboelectric nanogenerators based on flexible polyimide for energy harvesting and self-powered sensors, Nano Energy 109 (2023).

[57] F. Shi, et al., Electrospun polyimide nanofiber-based triboelectric nanogenerator for harvesting energy at elevated temperatures, ACS Appl. Electron. Mater. 4 (9) (2022) 4569–4575.

[58] L. Yang, et al., Preparation and characterization of a novel piezoelectric nanogenerator based on soluble and meltable copolyimide for harvesting mechanical energy, Nano Energy 67 (2020).

[59] H. Zou, et al., Quantifying the triboelectric series, Nat. Commun. 10 (1) (2019) 1427.

[60] Z. Ounaies, et al., Structure-property study of piezoelectricity in polyimides, in Smart Structures and Materials 1999: Electroactive Polymer Actuators and Devices, Y. BarCohen, Editor. 1999. p. 171-178.

[61] Z. Ounaies, et al., Dielectric properties of piezoelectric polyimides, in Materials for Smart Systems Ii, E.P. George, et al., Editors. 1997. p. 53-58.

[62] R.T. Leon, et al., Decoupling piezoelectric and triboelectric signals from PENGs using the fast fourier transform, Nano Energy 110 (2023).

[63] G. Collins, et al., Charge generation, charge transport, and residual charge in the electrospinning of polymers: A review of issues and complications, J. Appl. Phys. 111 (4) (2012).

[64] Z. Shi, et al., Thermo-processable polyimides with high thermo-oxidative stability as derived from oxydiphthalic anhydride and bisphenol A type dianhydride, High Perform. Polym. 12 (3) (2000) 377–394.

[65] K. Pramoda, et al., Characterization and thermal degradation of polyimide and polyamide liquid crystalline polymers, Polym. Degrad. Stab. 67 (2) (2000) 365–374.

[66] B. Cheng, et al., High performance temperature difference triboelectric nanogenerator, Nat. Commun. 12 (1) (2021) 4782.

[67] C. Xu, et al., On the electron-transfer mechanism in the contact-electrification effect, Adv. Mater. 30 (15) (2018) e1706790.

[68] S. Lin, et al., Electron transfer in nanoscale contact electrification: effect of temperature in the metal-dielectric case, Adv Mater 31 (17) (2019) e1808197.

[69] S. Khadtare, et al., A flexible piezoelectric nanogenerator using conducting polymer and silver nanowire hybrid electrodes for its application in real-time muscular monitoring system, Physical, Sensors and Actuators A, 2019, p. 299.

[70] K. Maity, et al., Self-powered human-health monitoring through aligned PVDF nanofibers interfaced skin-interactive piezoelectric sensor, ACS Appl. Polym. Mater. 2 (2) (2020) 862–878.

[71] H.H. Singh, N. Khare, Improved performance of ferroelectric nanocomposite flexible film based triboelectric nanogenerator by controlling surface morphology, polarizability, and hydrophobicity, Energy 178 (2019) 765–771.

[72] T. Huang, et al., Enhanced power output of a triboelectric nanogenerator composed of electrospun nanofiber mats doped with graphene oxide, Sci. Rep. 5 (2015).

[73] X.F. Kang, et al., Boosting performances of triboelectric nanogenerators by optimizing dielectric properties and thickness of electrification layer, RSC Adv. 10 (30) (2020) 17752–17759.

[74] J. Chun, et al., Mesoporous pores impregnated with Au nanoparticles as effective dielectrics for enhancing triboelectric nanogenerator performance in harsh environments, Energ. Environ. Sci. 8 (10) (2015) 3006–3012.

[75] M.K. Kim, et al., Wearable triboelectric nanogenerator using a plasma-etched PDMS-CNT composite for a physical activity sensor, RSC Adv. 7 (76) (2017) 48368–48373.

[76] C.M. Jiang, et al., A multifunctional and highly flexible triboelectric nanogenerator based on MXene-enabled porous film integrated with laser-induced graphene electrode, Nano Energy 66 (2019).

[77] D. Ali, et al., Enhancement of output performance through post-poling technique on BaTiO₃/PDMS-based triboelectric nanogenerator, Nanotechnology 28 (7) (2017).

[78] C.M. Jiang, et al., All-electrospun flexible triboelectric nanogenerator based on metallic MXene nanosheets, Nano Energy 59 (2019) 268–276.

[79] C. Wu, T.W. Kim, H.Y. Choi, Reduced graphene-oxide acting as electron-trapping sites in the friction layer for giant triboelectric enhancement, Nano Energy 32 (2017) 542–550.